CrossMark

ORIGINAL PAPER

Analysis of the strain process of soil slope model during infiltration using BOTDA

Jun-fan Yan[1] · Bin Shi[1] · Farhad Ansari[2] · Hong-hu Zhu[1] · Zhan-pu Song[1] ·
Ebrahim Nazarian[2]

Abstract Rainfall infiltration can be a major cause of slope failure. In the present paper, an indoor soil slope model was built; a distributed sensing fiber was designed based on Brillouin optical time-domain analysis (BOTDA). Two soil moisture probes were planted and a rainfall infiltrationtest was simulated to acquire the data of slope infiltration and deformation progress under rainfall infiltration. Time domain volumetric moisture content of the slope as well as the vertical and horizontal strain changes were monitored. The moisture content results showed the infiltration path and had obvious ascent at the sliding surface of the slope. The fiber results showed that there existed an apparent strain concentration near the shear section of the slope and strain conversion zone; the soil deformation law had a close spatial relationship with the infiltration path in the soil. In addition to the accurate determination of the sliding surface, a secondary shear surface was also detected by the BOTDA system. These results provide valuable information pertaining to the sliding mechanism and prediction of slope failure.

Keywords Soil slope · Distributed fiber optic sensing technology · Rainfall infiltration · Slope model test · BOTDA · Soil moisture content

✉ Bin Shi
  Shibin@nju.edu.cn

  Jun-fan Yan
  yjf880326@126.com

  Farhad Ansari
  fansari@uic.edu

  Hong-hu Zhu
  zhh@nju.edu.cn

  Zhan-pu Song
  zpsong@gmail.com

  Ebrahim Nazarian
  enazar2@uic.edu

[1] School of Earth Sciences and Engineering, Nanjing University, Nanjing 210023, China

[2] Department of Civil and Material Engineering, University of Illinois at Chicago, Chicago 60607, USA

Introduction

Rainfall infiltration, as one of the major inductions of slope failure, has been a subject of long-term research in the field of engineering geology (Aleotti and Chowdhury 1999; Canuti et al. 1985; Chen and Wang 2014; Duncan 1996; Finlay et al. 1997; Gasmo et al. 2000; Iverson and Major 1986; Iverson 2000; Li et al. 2005; Ng and Pang 2000; Ng and Shi 1998; Pradel and Raad 1993; Sugiyama et al. 1995; Zhang et al. 2014; Tang et al. 2015). Studies pertaining to slope stability and prediction of slope failures have been conducted in terms of variation and distribution of moisture and deformation fields inside the slope during rainfall infiltration (Lumb 1975; Brand et al. 1984; Au 1998; Crosta 1998; Tsai and Yang 2006; Cai and Ugai 2004; Collins and Znidarcic 2004; Rianna et al. 2014; Zhuang and Peng 2014). However, accurate predictions and monitoring methodologies are required for prediction of slope stability as they are key points in dealing with slope stability prediction and slope slide warning (Malet et al. 2002; Okada et al. 1994; Ranalli et al. 2014; Ranalli and Pagano et al. 2014; Suzuki and Matsuo 1988).

At present, hyetometers, water pressure gauges, displacement meters, settlement gauges and global positioning system (GPS) data are mostly used for local stress–strain and displacement monitoring of in situ slope stability

🖄 Springer

during rainfall infiltration, and slope stability evaluation (Alvioli et al. 2014; Alcántara-Ayala et al. 2012; Chen et al. 2014; Conte et al. 2010; Malet et al. 2002; Matsuura et al. 2003; Rianna et al. 2014; Tu et al. 2009). However, these methods mostly belong to point monitoring and are prone to undetected probability, which means the comprehensive process information of moisture and strain field may not be completely recorded. Meanwhile, point sensors are generally packaged with special materials such as metals or plastics, rendering the sensors bulky. The size mismatch between the oversized sensors and soil affect the accuracy of the monitored data. Therefore, the urgent problem is to develop some new sensing technology, which can monitor slope-related information during the process of rainfall infiltration and provide a reliable basis for an accurate assessment of slope stability.

Distributed fiber optic sensing (DFOS) is a class of distributed monitoring technology developed in recent years (Shi et al. 2007). In this technology, light is the information carrier and the fiber is the transmission medium that integrates sensing, transmission and measurement with continuous temporal and spatial information. Compared with traditional point-sensing technology, DOFS can realize distributed monitoring. Also, it has other outstanding advantages such as long-distance measurement, a flexible and slender shape, high durability, and corrosion and electromagnetic interference resistance. Based on these characteristics, a distributed network monitoring system can be easily built. In geological hazards prevention and slope engineering monitoring, DFOS has been applied more and more often (Wang et al. 2009, 2013; Zhu et al. 2014, 2015; Bai et al. 2014).

Some scholars have conducted a series of monitoring events during rainfall infiltration using DFOS technology. Huang et al. (2012) and Tan et al. (2013) used FBG technology to monitor in situ slopes and recorded the pore water pressure during rainfall infiltration, then studied the evaluation and development law of landslides and acquired some detailed information at specific points in the slope; however, the strain distribution condition was not acquired and, therefore, the results did not actually reflect the condition of the whole slope. Zeni et al. (2015) utilized BOTDA technology to monitor the strain in a model slope during rainfall infiltration, and obtained the abrupt information of the sensing fiber when slope failure just happened. However, in addition to the fiber slippage effect, the fiber was used at the surface of the slope and at depth. The strain varied at different depths and the maximum strain measured was only 200 με. Although these experiments are useful, further improvements can be employed.

The work presented in this study pertains to the determination of a deformation law for slopes during rainfall infiltration, and to capture and trace the mechanism for the deformation development process. An indoor rainfall infiltration test was designed for a slope model based on the measurements with BOTDA. It was possible to develop an accurate portrayal of the distributed strain and a moisture profile based on the monitored data.

Basic principle of BOTDA technology

The Brillouin optical time-domain analysis (BOTDA) used in the test is a distributed measurement technology. The operational principle of BOTDA is schematically shown in Fig. 1.

BOTDA is based on the stimulated Brillouin scattering (SBS) principle, which uses the linear relationship between the Brillouin scattering frequency variation (frequency shift) and the axial strain and/or temperature of a fiber to realize distributed sensing (Bao et al. 1995). The relationship can be expressed by the following equation:

$$v_B(\varepsilon, T) = v_B(\varepsilon_0, T_0) + \frac{\partial v_B(\varepsilon, T)}{\partial \varepsilon} \times (\varepsilon - \varepsilon_0) + \frac{\partial v_B(\varepsilon, T)}{\partial T} \times (T - T_0),$$

(1)

where $v_B(\varepsilon, T)$ and $v_B(\varepsilon_0, T_0)$ are frequency before and after measurement, respectively; ε and ε_0 are axial strain
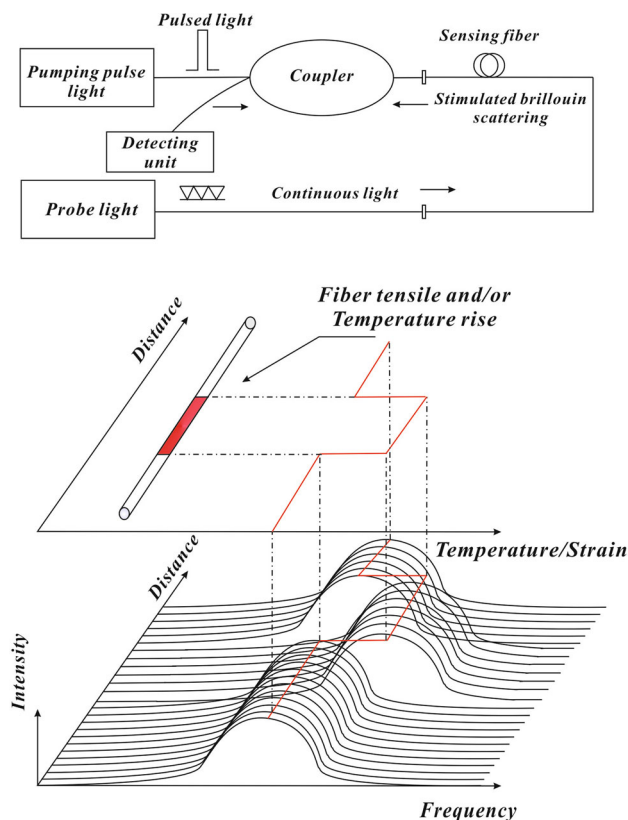

Fig. 1 Schematic diagram of the BOTDA sensing principle

Table 1 NBX-6050/A main performance indexes

Items	Performance indexes				
Distance range	50, 100, 250, 500 m; 1, 2.5, 5, 10, 25 km				
Range of strain measurement	$-30,000$ to $+40,000$ µε (-3 to 4 %)				
Readout resolution	5 cm (default), 1 cm (minimum)				
Pulse width	0.5 ns	1 ns	2 ns	5 ns	10 ns
Spatial resolution	5 cm	10 cm	20 cm	50 cm	100 cm
Measurement accuracy	15 µε	7.5 µε	7.5 µε	7.5 µε	7.5 µε

before and after measurement (it's an average strain at some certain spatial resolution); T and T_0 are the temperatures before and after measurement; the values of the proportional coefficient $\frac{\partial v_B(\varepsilon,T)}{\partial \varepsilon}$ and $\frac{\partial v_B(\varepsilon,T)}{\partial T}$ are 0.05 MHz/µε and 1.2 MHz/ºC, respectively.

During the monitoring process, BOTDA scans the entire length of the optical fiber for specified measurement parameters, i.e., intervals and spatial resolutions, and then the measured frequency shifts are converted to strain or temperature at each section based on Eq. (1). The optical fiber used in the system is commercially available telecommunication single mode fiber, which integrates sensing and transmission functions and is easily configured for real-time monitoring.

At present, the commercial demodulation instrument based on BOTDA can reach a spatial resolution of 5 cm, a measuring accuracy of 7µε, and a maximum measurement distance exceeding 25 km. The fiber layout can be adjusted in different ways to achieve either two-dimensional or three-dimensional measurements according to the practical needs. In the experiments performed in the present study, an NBX-6050/A demodulation instrument produced by the NEUBREX Company was used, where its specifications are given in Table 1. For the experiments performed in the present study, the spatial resolution, measurement accuracy and total measurement length were set to 10 cm, 7.5µε and 50 m, respectively.

Slope model test

Model device design

The experimental chamber shown in Fig. 2 was designed for determining the internal deformation of soil slopes during rainfall infiltration, tracking and capturing the formation and development of the sliding surface inside the slope.

The chamber is made of steel, with a length of 300 cm, width of 150 cm and height of 150 cm. The front side is ribbed glass with a spilt scale pasted at the corresponding position of sensing fiber for observing the slope deformation. The remaining three sides and bottom surface are

Fig. 2 Photograph of the model test chamber (unit: cm)

made of 10-mm-thick steel plates. An artificial slope model was built in the chamber, as well as a rectangular rainfall simulation chamber on the top of the slope model, with a length of 50 cm and width of 150 cm. The chamber is connected to a water supply device and the distance between the chamber and the slope crest is 20 cm. Simulation of rainfall is achieved by adjustable the water outlet in order to control the amount of rainfall infiltration. The schematics setup of the experiment is shown in Fig. 3.

Slope model and soil composition

The soil used for the test was a mixture of fine soil and kaolin; together with water, the mass ratio was 9:1:1. By particle size analysis, the average particle size of the sand was 0.5 mm, belonging to a well-graded sandy soil. The physical properties of the soil are shown in Table 2. The slope model was constructed by filling the chamber with the soil followed by compaction. The slope model was built to a height of 100 cm, width of 150 cm, slope bottom length of 300 cm, and at a slope angle of 45º as shown in Fig. 3.

Sensing fiber layout

The design and layout of sensing fiber is the key issue in BOTDA measurement. The fiber should be protected from

Fig. 3 Dimensions of the rainfall simulation device in the slope model test (unit: cm). (*1* Model test chamber; *2* Slope model; *3* Water discharge box; *4* Raining device; *5* Water pump; *6* Water tank; *7* Water pipe; *8* Bracket support; *9* Seepage control valve)
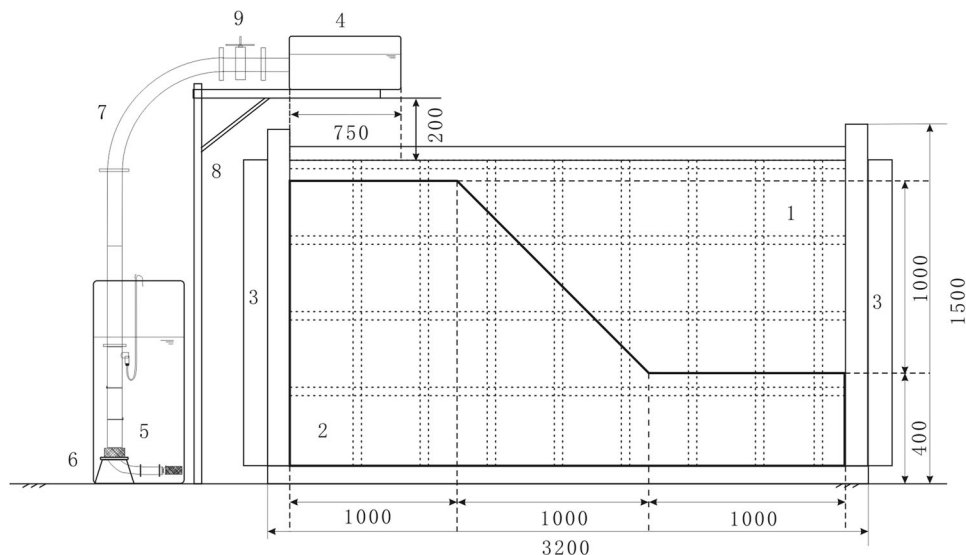

Table 2 Physical and mechanical parameters of soil material

Gravity	PC (m/s)[a]	Dry density (kN/m³)	Void ratio	Cohesion (kPa)		Internal friction angle (°)	
				Natural	Submerging	Natural	Submerging
2.63	4.0×10^{-5}	12.2	1.13	12.3	6.5	25.4	15.7

[a] Permeability coefficient

breakage and damage, and obtain valid data accurately as well. In the test, a 2-mm polyurethane, tight-buffered sensing fiber was used. The fiber was designed and produced by the authors and NanZee Sensing Technology Co., Ltd. at Suzhou. The fiber is elastic and extremely flexible, which makes it compatible with soil deformation and facilitates strain transfer between the soil and the sensor. The outside polyurethane fiber jacket has some advantages such as good abrasion resistance, anti-corrosion, insulation resistance and low temperature performance. It's Young's modulus is 0.3 Gpa, with a rigidity coefficient of 0.6×10^{6} N/m. In order to further improve the strain transfer mechanism between the fiber and the soil, 4-mm-thick heat-shrinkable tubes were adopted to improve the roughness of fiber and sensing sensitivity by increasing friction between fiber and the soil. The sensing fiber is schematically shown in Fig. 4.

Optical fiber sensors were placed in both horizontal and vertical layouts. Three horizontal layers of fibers were laid at depths of 70, 100 and 130, designated H1, H2 and H3, respectively. Each layer had four effective double-U-shaped sections. The lengths of H1, H2 and H3 along the X-axis were 140, 120 and 100, respectively. The vertical fiber was laid at the medium cross-section of the slope model; the layout of vertical fiber was also double-U-shape, named Z1 to Z4 from the leading to the trailing edge of the slope. The distances between each section and the
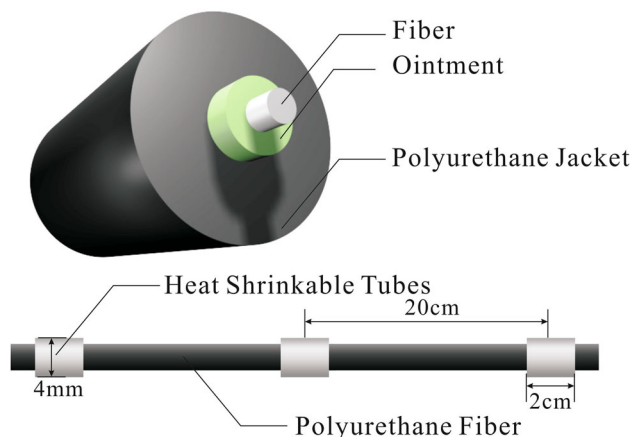

Fig. 4 Schematic diagram of sensing fiber

trailing edge were 100, 70, 40 and 10, respectively. The layout of sensing fiber in the model slope is shown in Fig. 5.

Because the bi-sensitivity of both strain and temperature of the BOTDA-based sensors, temperature compensation was needed before the tests. At selected positions within the model, a 2-meter-long redundant fiber was isolated and coiled and placed within a plastic box, within which the fiber would only be influenced by temperature. In addition to temperature compensation, the redundant fibers were also used for spatial localization. The boxes containing the

Fig. 5 Layout of the BOTDA sensing fiber in the model slope (unit: cm)
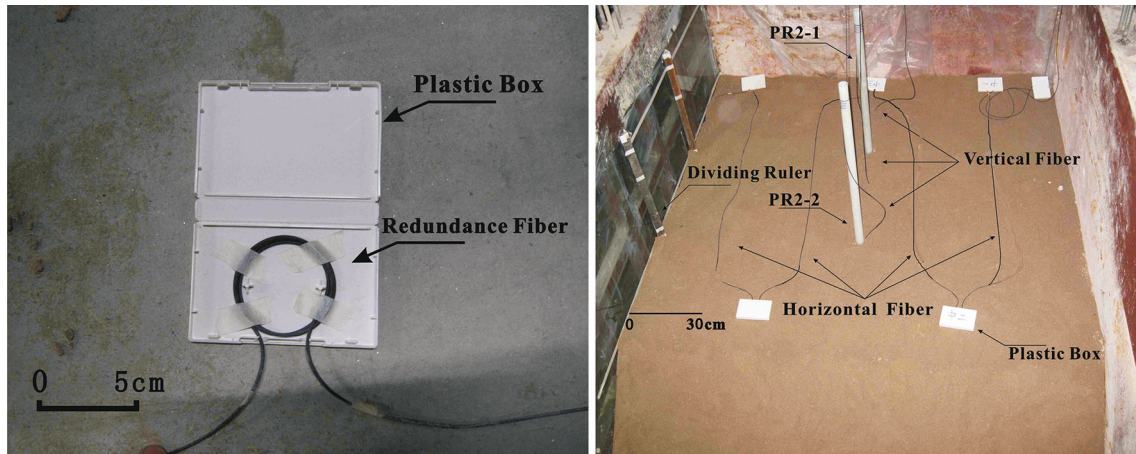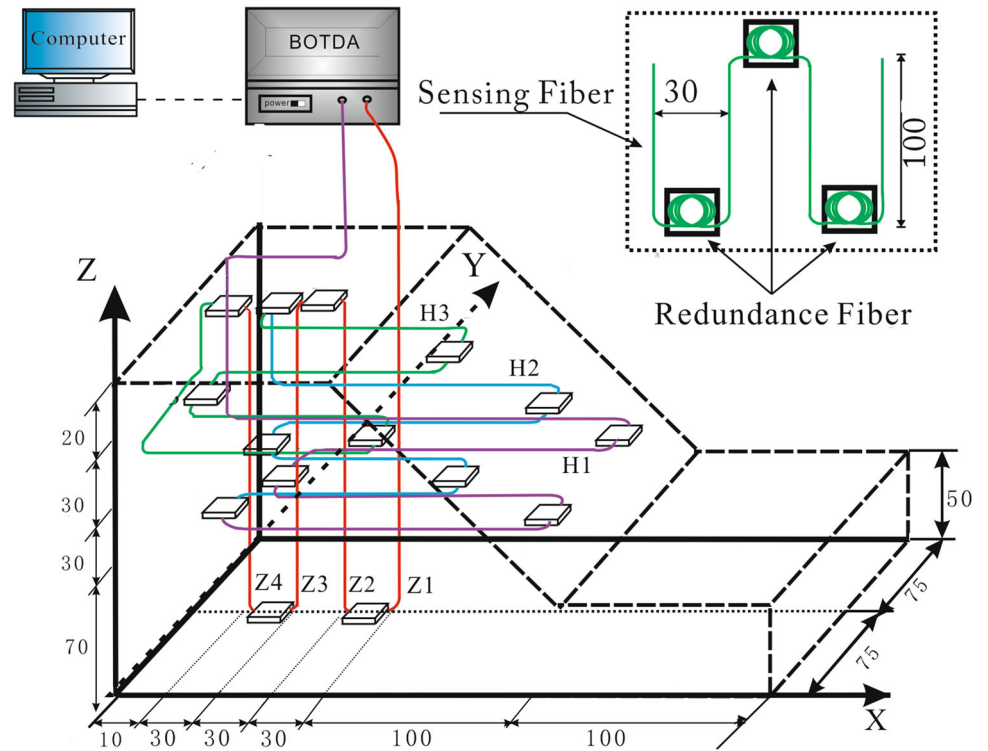
Fig. 6 Photos of the installation of the BOTDA fiber network. [Sensing fiber and the coiled redundant optical fiber in the box (*left*); installed optical fibers in the slope model (*right*)]

redundant temperature compensation optical fibers are shown in Fig. 6.

Slope moisture measurement

For slope monitoring, moisture is also a basic parameter to be measured (Tohari et al. 2007; Huang et al. 2008). At this in-door test, moisture measurements at different depths of the slope model were made by two PR2 profile probes (Delta-T Devices, Ltd.). These probes possess the capability for real-time monitoring of the soil moisture at various segments along the depth. The PR2 probes were produced by Delta-T Devices, Ltd. By using the PR2 probes, it was possible to monitor the moisture volume at the depths of 20, 30, 40, 60 and 100 cm. The range of measurements for the probes was from 0.04 m^3/m^3 to 0.4 m^3/m^3, with a measuring accuracy of 0.04 m^3/m^3. The two probes were inserted into the soil at the central axis (C/A) of the slope, and the 100-cm sensor was flushed to the slope toe, so that the distance between the slope top and the top sensor (20 cm) was also 20 cm. One probe was planted at the juncture of the infiltrated and dry areas, (designated
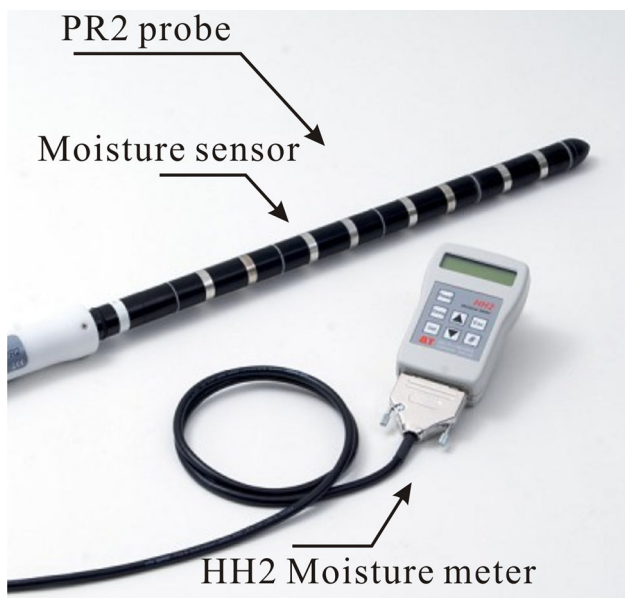
Fig. 7 PR2 soil moisture profile probe

as PR2-1); the other probe was placed at the interface between the slope top surface and the inclined surface, designated as PR2-2. Figure 7 pertains to the photo of the moisture probe, and the layout scheme for the probes is shown in Fig. 8.

The experiments process

The experiments were carried out with the instrumentation shown in Fig. 3. The total amount of rainfall infiltration was controlled by the method discussed in an earlier section of this article. The rainfall duration for each level lasted for 3 h (hours), with the intensity ranging from

0 mm/day to 196 mm/day, and increased by 9.8 mm/day per level. In doing so, it was possible to simulate a range of rain scenarios from very low (0.1–10 mm/day) to heavy rain (150–200 mm/day). The measurement points were selected based on the computation of the rainfall uniformity according to the following relationship:

$$C_u = 100 \times \left(1 - \frac{\sum |x|}{m \times n} \right) \qquad (2)$$

where C_u is rainfall uniformity, m is the total rainfall amount in unit time; n is the total number of test points; x is the difference between each value and average value. To achieve rainfall uniformity greater than 90 %, 16 measuring points were selected for rainfall uniformity evaluation, where the amount of rainfall for 1-min duration at each point was compared with the average amount.

The sampling rate for the acquisition of moisture data for infiltration rates lower than 80 mm/day was once every 2.5 h. For larger infiltration rates as the rate of rainfall gradually increased (80–196 mm/day), data was collected every hour. The sampling rate was increased to half-hour intervals, once the rainfall infiltration rate stabilized at 196 mm/day. These steps were done both for moisture as well as distributed strain sensors in order to accurately portray the deformation and strain distribution of the soil profile.
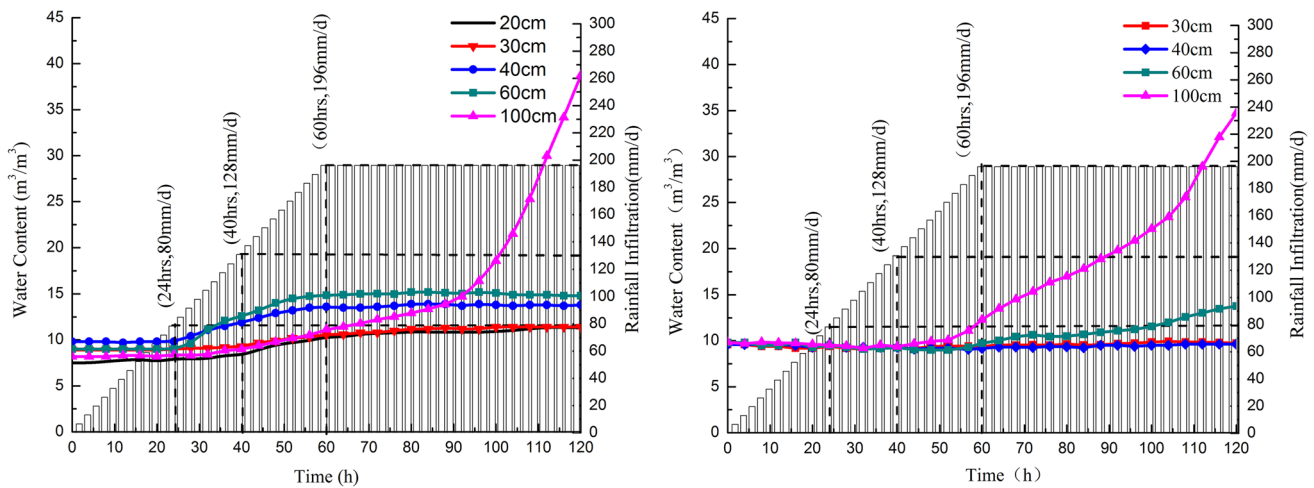
Measurement results and analysis

PR2 soil moisture results

The measured time-history curves of soil volume moisture at different depths are shown in Fig. 9. To facilitate further analysis, 4 particular moisture contents at 24, 40, 60 and 120 h were selected, and presented in Table 3.

Fig. 8 Dimensions of the slope model (unit: cm)
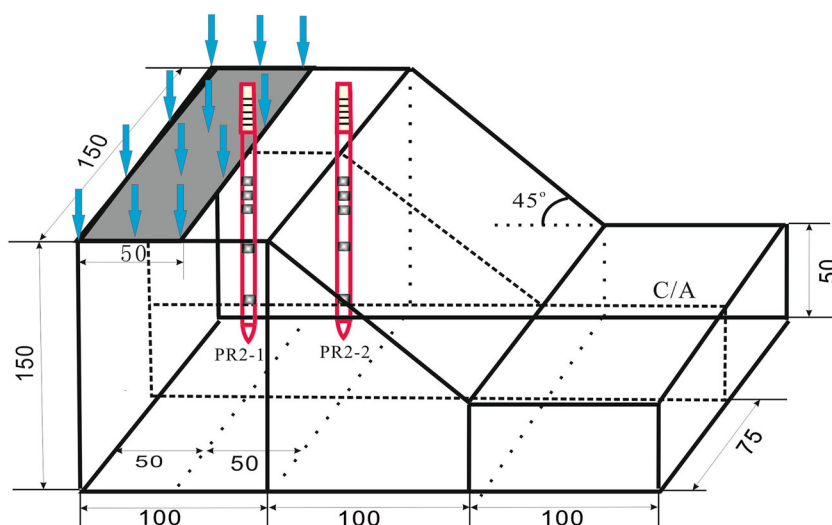
Fig. 9 Time-history curves of volume moisture content by PR2

Table 3 Volume moisture content measured at times of 24, 60 and 120 h by PR2 (unit: m³/m³)

Time	20 cm		30 cm		40 cm		60 cm		100 cm	
	PR2-1	PR2-2	PR2-1	PR2-2	PR2-1	PR2-2	PR2-1	PR2-2	PR2-1	PR2-2
24 h	0.078	N/A	0.082	0.094	0.088	0.096	0.090	0.095	0.084	0.095
40 h	0.080	N/A	0.086	0.095	0.116	0.094	0.124	0.094	0.086	0.094
60 h	0.105	N/A	0.106	0.094	0.136	0.095	0.147	0.116	0.126	0.146
120 h	0.106	N/A	0.114	0.095	0.137	0.095	0.149	0.179	0.385	0.331

As shown in Table 3, results from moisture measurements by PR2-2 moisture meter sensor at 20 cm were not recorded, since the moisture content of the soil at the 20-cm level is lower than PR2's measurement range. By analysis of Table 3 and Fig. 9, some conclusions can be drawn. Within the first 24 h, rainfall infiltration was less than 80 mm/day; therefore, except for the 30–60 cm range as measured by PR2-1, the change in moisture content was low. These results indicated that the surrounding soil was also in the infiltration stage with little or no change in moisture content.

During the period of 24–40 h, the amount of rainfall infiltration was between 80 mm/day to 128 mm/day. According to the five sampling points at PR2-1, the volumetric moisture content of the soil was slightly increased near the infiltration area. The largest increase appeared at depths of 60 cm (0.124 m³/m³) and 40 cm (0.116 m³/m³). The PR2-2 probe, which was placed far away from the infiltration area, didn't exhibit any noticeable changes.

Examination of data during the period between 40 and 60 h reveals that the rainfall infiltration increased from 128 mm/day to 196 mm/day. Therefore, the moisture content depths of 20, 30 and 100 at PR2-1 increased to 0.105, 0.106 and 0.126 m³/m³, respectively. However, larger increases were still at the depths of 60 cm and 40 cm, reaching 0.147 and 0.136 m³/m³, respectively. At the depth of 100 cm (bottom), the moisture content was the highest at 0.146 m³/m³. Following an infiltration period of 55 h, the only further increase in the moisture content was at 60 cm (0.116 m³/m³). In essence, according to the sensor data, after nearly 60 h, moisture totally permeates to the bottom of the model soil and causes lateral runoff.

Finally, during the period of 60 to 120 h, rainfall infiltration increased to 196 mm/day. Moisture content increased during this period at the depth of 100 cm as measured by PR2-1 and ultimately reached 0.385 m³/m³. Moisture content at other positions for the same sensor remained stable. Results from PR2-2 also indicated that at the depths of 100 and 60 cm, moisture contents exhibited increases to 0.33 and 0.149 m³/m³, ultimately. These results indicate that 120 h of simulated rainfall saturates the bottom level of the soil model. During this same time period, the upper sections remained unsaturated.

Based on the above-mentioned results and analysis, some conclusion can be generalized: during early periods of the simulated rainfall infiltration process, seepage performance was vertical infiltration, directly into the bottom of the model, the bottom part of soil moisture content continuously improved, and the soil became saturated gradually, and produced lateral runoff after soil saturation. The variation of soil moisture content is closely related to infiltration paths.

BOTDA strain results

Strain results of the horizontal optic fiber

As discussed earlier, the horizontal fiber optic sensors were placed at three levels, covering the lower, middle and upper altitudes of the soil model. Figure 10a–c pertains to the strain distribution of the upper (H3), middle (H2) and lower (H1) layers following temperature compensation by the data from the redundant optical fiber. The shaded area depicts the rainfall infiltration area. Considering that each of the distributed sensors at the three altitudes consist of four sections, their average response at 1, 12 and 24 h is shown in Fig. 11. Lines L and L' correspond to the strain concentration locations for H3 and H2, respectively, when rainfall infiltration reached 196 mm/day.

Analysis of the horizontal strain data at the three layers H1, H2 and H3 shown in Fig. 11 indicates that: (1) strain at the bottom layer of the slope model basically remains negligible, pointing to the fact that the rainfall infiltration does not strain the lower section; (2) in this test, rainfall infiltration had little effect on the bottom part of the slope model. The four sections of sensing fiber at the level of H2 in the infiltration area showed significant tensile strains with increase in infiltration: tensile strains in the range of 400–700 $\mu\varepsilon$ were experienced at the infiltration area. Strains at the non-infiltration section of H2 were also tensile, but within a lower range of 200–400 $\mu\varepsilon$. At the level pertaining to H3, in consonance with H2, the tensile strains in the infiltration area increased with the volume increase in rainfall. However, the model slope experienced a strain transition in the infiltration area, where tensile strains were transitioned to a compressive domain (300 $\mu\varepsilon$). Furthermore, analysis of the four sections of the distributed sensor at each of the three levels H1, H2 and H3 in Fig. 10 indicates the differences in strains at the same level due to boundary conditions and unevenness of the infiltration process.

The axial strains generated in H1, H2 and H3 pertain to the expansion and contraction of the soil and their respective elevations within the slope model. Strains measured by H1 were negligible due to the fact that the slope model was confined on the sides and the soil was not able to expand due to the boundaries and to contract due to confinement of the moisture at the elevation.

The larger tensile strains in the infiltration zone measured by H2 are due to the weakening of the soil due to increase in moisture content. Lateral deformation of the soil in the infiltration area was much larger than the dry non-filtration zone, because of the differences in moisture content. Nevertheless, the non-infiltration zone also exhibited lateral displacement (expansion) because of its vicinity to the free surface of the slope. Tensile strains in

H3 were also indicative of moisture-related soil expansion in the infiltration zone. The non-filtration section of this layer contracted as demonstrated by the compressive strains, because of the shrinkage associated with dehydration and evaporation at this upper level.

Strain results of the vertical optic fiber

As shown in Fig. 12, vertical strains were either zero or very low in the infiltration zone as shown by Z4 and Z3, respectively. The vertical strains went through a tensile-to-compressive transition (upper to lower) within each section in the infiltration zone, identified by C and D on Z3. On the other hand, strains from the sensors in the non-filtration zone, Z1 and Z2, exhibited larger strains with a change in polarity form compressive-to-tensile (upper to lower). The 750-$\mu\varepsilon$ compressive strain converted to 700-$\mu\varepsilon$ tensile strain at the depth of 100 cm, and followed by Z2, 400 $\mu\varepsilon$ at the depth of 105 cm, and was converted to tensile strain at the intersection of H2, then developed to a maximum of about 550 $\mu\varepsilon$ (A) at a depth of 80 cm. Z2 had a similar compressive to tensile strain conversion trend as Z1, but the corresponding strains were smaller than Z1; it began to produce compressive strain at the depth of 130 cm, reached a maximum strain of 400 $\mu\varepsilon$ at the depth of 115 cm, and was converted to tensile strain, then developed to a maximum of about 250 $\mu\varepsilon$ at the depth of 105 cm(B); Z3 was in the rainfall infiltration area, it had two strain conversion districts opposite to (A) and (B). One was at the top of the slope. A tensile to compressive strain conversion occurred at a depth of 150 to 110 cm; the maximum tensile and compressive strains were 180 and 140 $\mu\varepsilon$, respectively (C). The other tensile-to-compressive strain conversion occurred at the depth of 105 to 80 cm. The maximum tensile strain was 160 $\mu\varepsilon$ at the depth of 95 cm and the maximum compressive strain was 210 $\mu\varepsilon$ at the depth of 80 cm (D).

Considering the position of strain conversion districts of Z1, Z2 and Z3, a shear zone (sliding surface) would be confirmed by linking them with a dotted line. And the sublevel shear plane at Z3's lower portion of strain conversion district was caused by localized shear deformation; it couldn't form a complete shear zone without other shear deformation.

Mechanism of infiltration and deformation

Examination of the experimental results reveals direct correlation between moisture content, the measured strains, and formation of a slip surface. Progression of moisture from the infiltration stage to the runoff state over the period of measurement was manifested through development of a
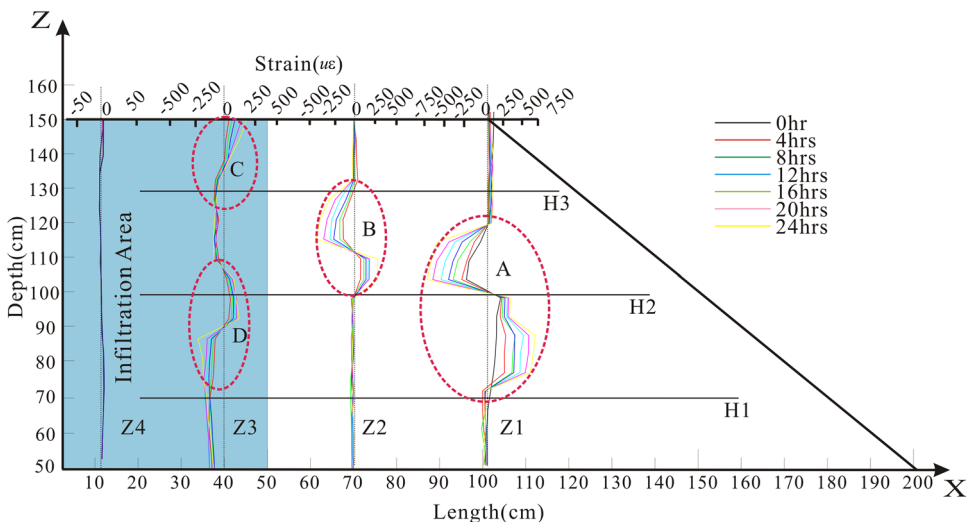
Fig. 10 Strain monitoring results of three layers in the slope
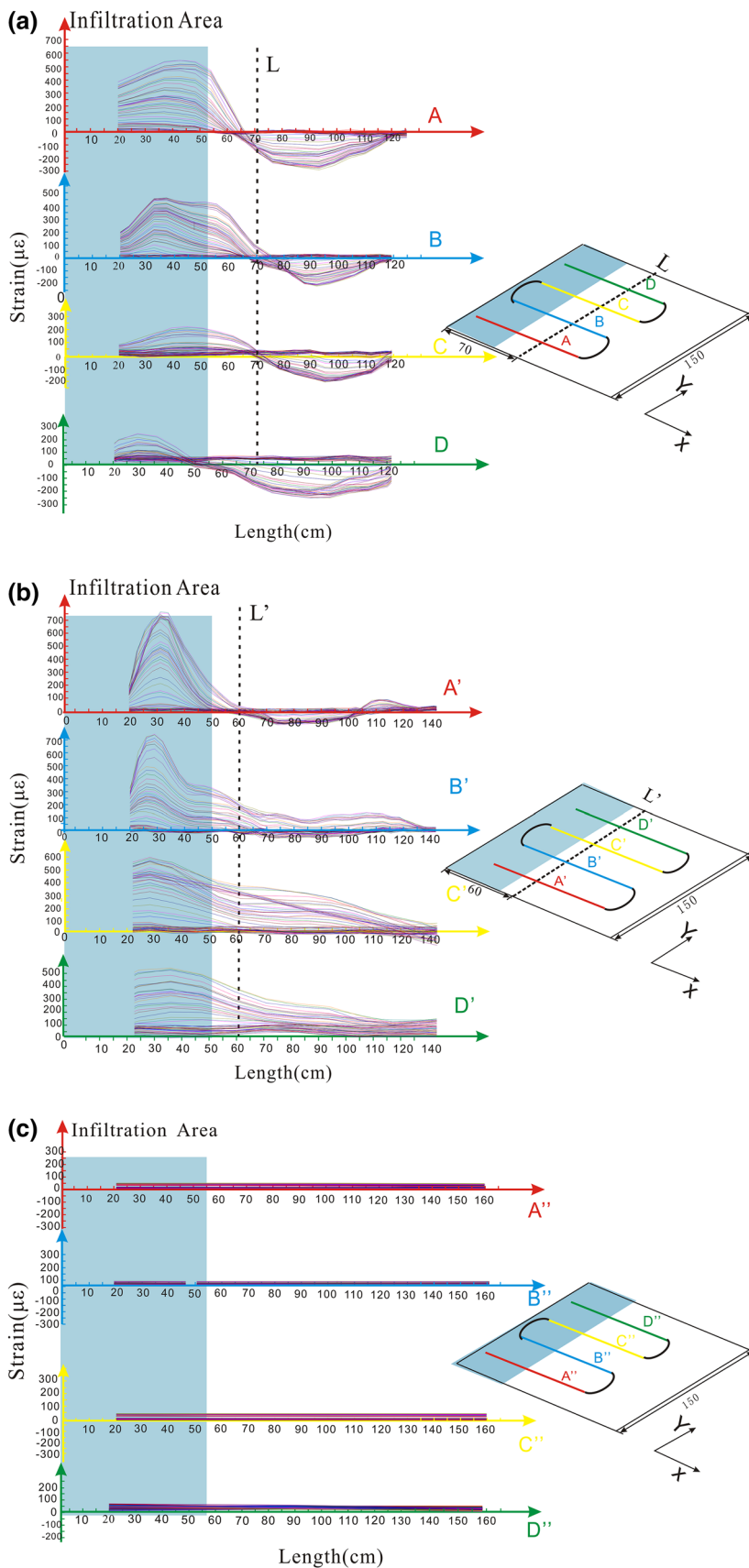
Fig. 11 The strain monitoring results of the sensing fiber section in three layers at 1, 12 and 24 h after rainfall infiltration reached 192 mm/day
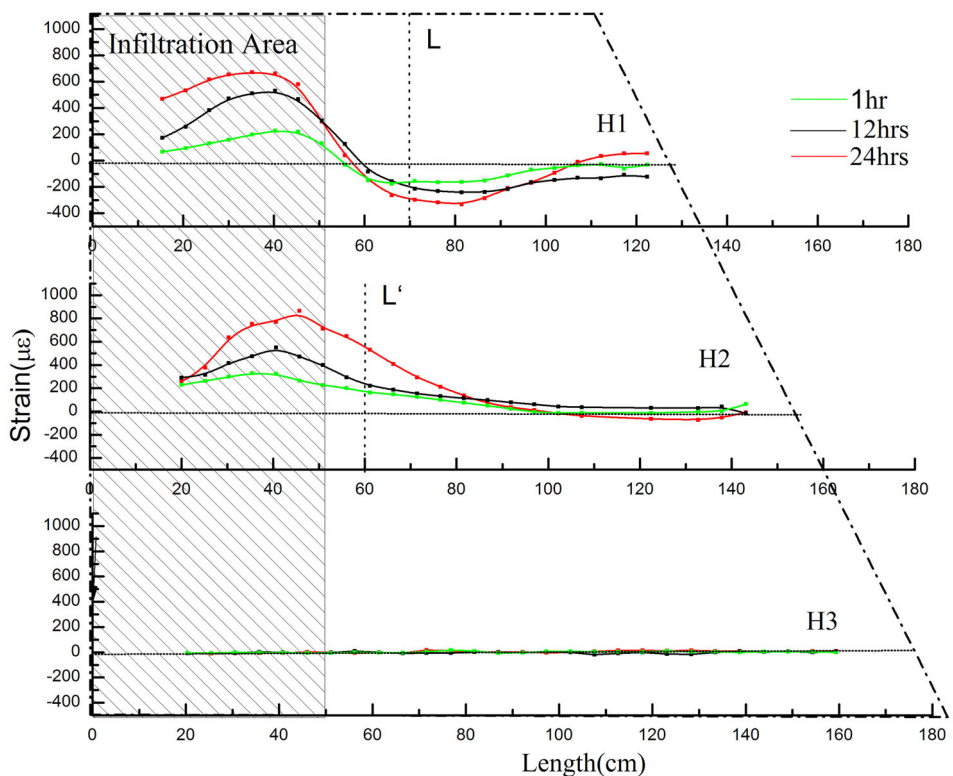

Fig. 12 Strain monitoring results of vertical fiber in the slope

moisture path at lower depths (60–100 cm), and infiltrated moisture near the surface of the infiltration zone. Analysis of horizontal strain data also indicated the locations for which the soil had either contracted or expanded due to moisture, evaporation and boundary conditions. The horizontal strain data provided qualitative correlation between soil deformation and the path of rainfall infiltration with the position in slope. Analysis of vertical measurements of strain provides more detailed information about the slip surface.

Experimental results also allowed for prediction of the sliding surface. As discussed earlier, within the sloped section of the model, the upper levels were fully dry and lower levels were saturated by the runoff. Therefore, the soil was stronger at the upper levels and weaker at the lower. The transition zone, from compressive at upper to tension at lower levels, at each section alone the length of the slope model would contribute to formation of a shear slip zone as demonstrated from the results shown by Z1 and Z2 in Fig. 12. Interconnection of a series of shear

Fig. 13 Measured and calculated slip surface of the slope (unit: cm)
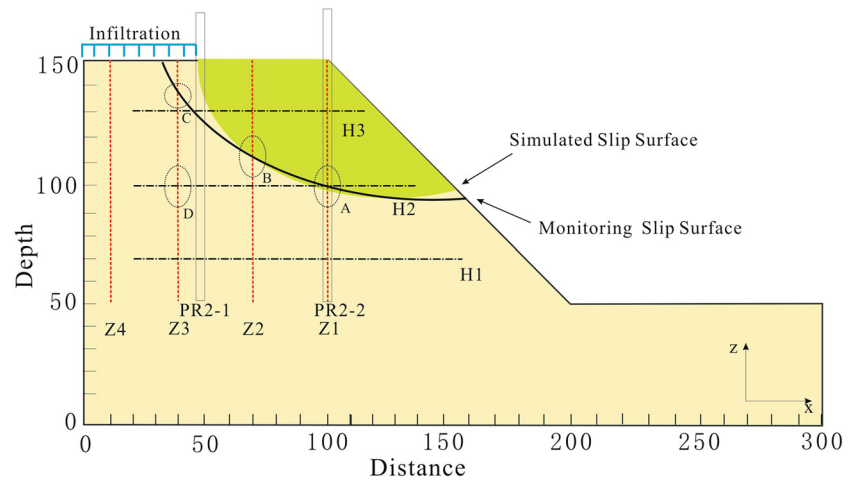
zones is responsible for creation of a sliding surface, a precursor to landslides. An increase in moisture content at the lower sections creates tension in the fiber, whereas the evaporation of moisture at the higher levels results in contraction and compression as indicated by Z1 and Z2 in Fig. 12. Conversely, within the sections directly in the infiltration zone, the upper sections exhibit tension because of prolonged immersion in water and. therefore, the strain transition is from tension to compression as shown by Z3 in Fig. 12. By connecting the transition zones as determined by Z1 through Z3, it will be possible to establish the shear zone or the sliding surface for the slope.

Verification of the above-mentioned findings were accomplished through numerical modeling of the slope by using the SLOPE/W and SEEP/W simulation software and the Morgenstern–Price method. The model was established by considering a two-dimensional plane strain problem. As shown in Fig. 13, the experimental and numerically computed sliding surface compared well.

The test results show that the distributed fiber optic monitoring technology based on BOTDA has obvious advantages over the general point monitoring technology. It not only monitored the strain shear zone near the strain conversion district, but also captured some sub-level shear plane data; the test results had great significance on the study of the formation mechanism, forecasting and early warming of landslides.

Conclusion

In this paper, an in situ rainfall infiltration test based on BOTDA was undertaken on a model slope. The main conclusions drawn from the study are as follows:

1. The internal horizontal and vertical strains in slope were distributionally monitored during rainfall infiltration. The strain conversion district was monitored near the shear zones, and the formation mechanism of a landslide was analyzed. This research has important significance for forecasting and early warnings of landslides.

2. The rainfall infiltration path could be acquired and analyzed by obtaining the variation of volume moisture of soil using PR2 moisture probes during the test. In field work, it's also a convenient method to collect some infiltration information.

3. The 2-mm polyurethane, tight-buffered sensing fiber used in the test can effectively fulfill soil deformation monitoring; its unique advantages makes this fiber very suitable in field work. The three-dimensional internal deformation of the slope model was accurately obtained through horizontally and vertically laid distributed fiber measurement, which provides a reliable basis for further analysis of slope stability.

4. The test results showed that the deformation of a slope is closely related to the location and the path of rainfall infiltration. The mechanism of their interaction was analyzed in the paper.

5. The finite element numerical simulation analysis proved the accuracy of the results by BOTDA-distributed optical fiber monitoring. The test results also showed that, based on BOTDA technology, not only the main sliding zone can be determined in the slope, but also the sub-level shear plane can be captured. This newly developed technology is full of great significance in studying the formation mechanism, forecasting and early warnings of landslides.

References

Alcántara-Ayala I, López-García J, Garnica RJ (2012) On the landslide event in 2010 in the Monarch Butterfly Biosphere Reserve, Angangueo, Michoacán, Mexico. Landslides 9(2):263–273

Aleotti P, Chowdhury R (1999) Landslide hazard assessment: summary review and new perspective. Bull Eng Geol Environ 58(1):21–44

Alvioli M, Guzzetti F, Rossi M (2014) Scaling properties of rainfall induced landslides predicted by a physically based model. Geomorphology 213:38–47

Au SWC (1998) Rain-induced slope instability in Hong-Kong. Eng Geol 51:1–36

Bai SB, Wang J, Thiebes B, Cheng C, Yang YP (2014) Analysis of the relationship of landslide occurrence with rainfall: a case study of Wudu County, China. Arab J Geosci 7:1277–1285

Bao X, Dhliwayo J, Heron N, Webb DJ, Jackson DA (1995) Experimental and theoretical studies on a distributed temperature sensor based on Brillouin scattering. J Lightwave Tech 13(7):1340–1348

Brand EW, Premchitt J, Phillipson HB (1984) Relationship between rainfall and landslides in Hong Kong. In: Canadian Geotechnical Society (ed.) Proceeding of 4th international symposium on landslides. 1:377–384

Cai F, Ugai K (2004) Numerical analysis of rainfall effects on slope stability. Int J Geomech 4:69–78

Canuti P, Focardi P, Garzonio CA (1985) Correlation between rainfall and landslides. Bull Eng Geol Environ 32(1):49–54

Chen HX, Wang JD (2014) Regression analyses for the minimum intensity-duration conditions of continuous rainfall for mudflows triggering in Yan'an, northern Shaanxi (China). Bull Eng Geol Environ 73(4):917–928

Chen KT, Kuo YS, Shieh CL (2014) Rapid geometry analysis for earthquake-induced and rainfall-induced landslide dams in Taiwan. J Mt Sci 11(2):360–370

Collins BD, Znidarcic D (2004) Stability analyses of rainfall induced landslides. J Geotech Geoenviron Engi 130(4):362–372

Conte E, Silvestri F, Troncone A (2010) Stability analysis of slopes in soils with strain-softening behavior. Comput Geotech 37:710–722

Crosta G (1998) Regionalization of rainfall thresholds: an aid to landslide hazard evaluation. Eng Geol 35(2–3):131–145

Duncan JM (1996) State of the art: limit equilibrium and finite-element analysis of slopes. Geotech Eng 122:577–596

Finlay PJ, Fell R, Maguire PK (1997) The relationship between the probability of landslide occurrence and rainfall. Can Geotech J 34(6):811–824

Gasmo JM, Rahardjo H, Leong EC (2000) Infiltration effects on stability of a residual soil slope. Comput Geotech 26:145–165

Huang CC, Lo CL, Jang JS (2008) Internal soil moisture response to rainfall-induced slope failures and debris discharge. Eng Geol 101(3):134–145

Huang AB, Lee JT, Ho YT, Chiu YF, Cheng SY (2012) Stability monitoring of rainfall-induced deep landslides through pore pressure profile measurement. Soils Found 52(4):737–747

Iverson RM (2000) Landslide triggering by rain infiltration. Water Resour Res 36(7):1897–1910

Iverson RM, Major JJ (1986) Groundwater seepage vectors and the potential for hillslope failure and debris flow mobilization. Water Resour Res 22(11):1543–1548

Li AG, Tham LG, Yue ZQ, Lee CF, Law KT (2005) Comparison of field and laboratory soil–water characteristic curves. J Geotech Geoenviron Eng 131(9):1176–1179

Lumb P (1975) Slope failures in Hong Kong. Q J Eng Geol Hydroge 8(1):31–65

Malet JP, Maquaire O, Calais E (2002) The use of global positioning system techniques for the continuous monitoring of landslides: application to super-sauze earthflow (Alpes-de-Haute-Province, France). Geomorphology 43(1–2):33–54

Matsuura S, Asano S, Okamoto T (2003) Characteristics of the displacement of a landslide with shallow sliding surface in a heavy snow district of Japan. Eng Geol 69(1–2):15–35

Ng CWW, Pang YW (2000) Influence of stress state on soil-water characteristics and slope stability. J Geotech Geoenviron Eng 126(2):157–166

Ng CWW, Shi Q (1998) A numerical investigation of the stability of unsaturated soil slopes subjected to transient seepage. Comput Geotech 22:1–28

Okada K, Sugiyama T, Muraishi H, Noguchi T, Samizo M (1994) Statistical risk estimating method for rainfall on surface collapse of a cut slope. Soils Found 34:49–58

Pradel D, Raad G (1993) Effect of permeability on surficial stability of homogeneous slopes. J Geotech Eng 119:315–332

Ranalli M, Medina-Cetina Z, ASCE SM, Gottardi G, Nadim F (2014) Probabilistic calibration of a dynamic model for predicting rainfall-controlled landslides. J Geotech Geoenviron Eng 140:04013039

Rianna G, Pagano L, Urciuoli G (2014) Rainfall patterns triggering shallow flowslides in pyroclastic soils. Eng Geol 174:22–35

Shi B, Zhang D, and Wang BJ (2007) Distributed optical fiber monitoring technology of geological and geotechnical engineering and its development. J Eng Geol 15(S2):109–116 (in Chinese)

Sugiyama T, Okata K, Muraishi H, Noguchi T, Samizo M (1995) Statistical rainfall risk estimating method for a deep collapse of a cut slope. Soils Found 35(4):37–48

Suzuki H, Matsuo M (1988) Procedure of slope failure prediction during rainfall based on the back analysis of actual case records. Soils Found 28(3):51–63

Tan DJ, Han B, Li LL (2013) Study on the application of fbg technology in rainfall monitoring. Adv Mater Res 668:959–963

Tang HM, Li CD, Hu XL, Wang LQ, Criss R, Su AJ, Wu YP, Xiong CR (2015) Deformation response of the Huangtupo landslide to rainfall and the changing levels of the Three Gorges reservoir. B Eng Geol Environ 74(3):933–942

Tohari A, Nishigaki M, Komatsu M (2007) Laboratory rainfall-induced slope failure with moisture content measurement. J Geotech Geoenviron Eng 133(5):575–587

Tsai TL, Yang JC (2006) Modeling of rainfall-triggered shallow landslide. Environ Geol 50:525–534

Tu XB, Kwong AKL, Dai FC (2009) Field monitoring of rainfall infiltration in A Loess slope and analysis of failure mechanism of rainfall-induced landslides. Eng Geol 105(1):134–150

Wang BJ, Li K, Shi B (2009) Test on application of distributed fiber optic sensing technique into soil slope monitoring. Landslide 6(1):61–68

Wang JJ, Liang Y, Zhang HP, Wu Y, Lin X (2013) A loess landslide induced by excavation and rainfall. Landslide 11:141–152

Zeni L, Picarelli L, Avolio B, Coscetta A, Papa R, Zeni G, Di Maio C, Vassallo R, Minardo A (2015) Brillouin optical time-domain analysis for geotechnical monitoring. J Rock Mech Geotech Eng 7(4):458–462

Zhang J, Huang HW, Zhang LM, Zhu HH, Shi B (2014) Probabilistic prediction of rainfall-induced slope failure using a mechanics based model. Eng Geol 168(1):129–140

Zhu HH, Shi B, Zhang J, Yan JF, Zhang CC (2014) Distributed fiber optic monitoring and stability analysis of a model slope under surcharge loading. J Mt Sci 11(4):979–989

Zhu HH, Yan Shi B, Zhang JF, Wang J (2015) Investigation of the evolutionary process of a reinforced model slope using a fiber-optic monitoring network. Eng Geol 186:34–43

Zhuang JQ, Peng JB (2014) A coupled slope cutting- a prolonged rainfall-induced loess landslide: a 17 October 2011 case study. Bull Eng Geol Environ 73(4):997–1011